Delft University of Technology

Growth-ring effect on moisture-induced stress and damage development in glued laminated timber

Yu, Taoyi; Seeber, Franziska; Khaloian, Ani; van de Kuilen, Jan Willem

DOI
10.1007/s00226-025-01647-5

Publication date
2025

Document Version
Final published version

Published in
Wood Science and Technology

Citation (APA)
Yu, T., Seeber, F., Khaloian, A., & van de Kuilen, J. W. (2025). Growth-ring effect on moisture-induced stress and damage development in glued laminated timber. *Wood Science and Technology*, *59*(4), Article 58. https://doi.org/10.1007/s00226-025-01647-5

Important note
To cite this publication, please use the final published version (if applicable).
Please check the document version above.

Copyright
Other than for strictly personal use, it is not permitted to download, forward or distribute the text or part of it, without the consent of the author(s) and/or copyright holder(s), unless the work is under an open content license such as Creative Commons.

Takedown policy
Please contact us and provide details if you believe this document breaches copyrights.
We will remove access to the work immediately and investigate your claim.

This work is downloaded from Delft University of Technology.
For technical reasons the number of authors shown on this cover page is limited to a maximum of 10.

Wood Science and Technology (2025) 59:58
https://doi.org/10.1007/s00226-025-01647-5

ORIGINAL

Growth-ring effect on moisture-induced stress and damage development in glued laminated timber

Taoyi Yu[1,2] · Franziska Seeber[1,2] · Ani Khaloian[1] · Jan-Willem van de Kuilen[1,3]

Received: 13 August 2024 / Accepted: 28 February 2025
© The Author(s) 2025

Abstract

Humidity fluctuations are a leading cause of damage in wooden constructions. In the case of glulam products, the multitude of possible layups concerning pith locations, diverse material properties across wood species, and the high computational cost associated with multi-field analysis have constrained many research efforts to focus on one specific glulam layup, consequently limiting the generalizability of the findings. To address this challenge, Monte Carlo simulations were employed to assess the significance of various factors. Based on which, two levels of simplification are proposed. The first level reduces the multi-layer problem to a single-layer one by applying appropriate boundary conditions. It substantially reduces the simulation costs and consequently facilitates sophisticated damage analysis, revealing the varying damage pattern across different board types. The second level of simplification further reduces the problem to a single-element model, enabling an analytical estimation of moisture stress. This level of simplification elucidates how factors such as moisture difference, material rotational angle, and other material properties influence the moisture-induced stress. Most importantly, it facilitates a rapid estimation of the critical moisture fluctuation range and the preferred sawing location of boards for different wood species, which can provide guidance to the production of higher moisture resistant glulam.

List of symbols

α_i	Hydro-expansion coefficient (−), i = R, T, L

✉ Taoyi Yu
yu@hfm.tum.de

1 Department of Materials Engineering, School of Engineering and Design, Technical University of Munich, Munich, Germany

2 International Graduate School of Science and Engineering, Technical University of Munich, Munich, Germany

3 Biobased Structures and Materials, Faculty of Civil Engineering and Geosciences, Delft University of Technology, Delft, The Netherlands

Published online: 08 May 2025

$\boldsymbol{\epsilon}_{P/Center}^{initial/free/end}$	Strain of element P/Center at initial/virtual-free-shrinkage/end state in Fig. 12 (−)
$\boldsymbol{\sigma}_{P/Center}^{initial/free/end}$	Stress of element P/Center at initial/virtual-free-shrinkage/end state in Fig. 12 (MPa)
$\boldsymbol{C}$	Stiffness tensor
$\boldsymbol{T}^{\epsilon/\sigma}$	Transformation matrix for strain/stress
v_{ij}	Poisson's ratio (−)
ρ	Density (g/mm^3)
$\mathbf{f}$	Moisture flux tensor (g s^{-1} mm^{-3})
θ	Material rotational angle
$d_{t/v,i}$	Damage variable (for tension/shear) in direction i
E_i	Young's modulus in direction i (MPa)
f_i	Strength in direction i (MPa)
$F_{t/v,i}$	Damage initiation criteria (for tension/shear) in direction i
G_{ij}	Shear modulus (MPa)
J	Moisture flux across the surface (g s^{-1} mm^{-2})
LOC_i	Location i to surface, i = 1, 2, 3..., illustrated in Fig. 5
S_u	Surface emission coefficient (mm/s)
t	Time (s)
u	Moisture content (−)
u_{EMC}	Equilibrium moisture content (−)
D	Diffusion coefficient (mm$^2/s$)

Introduction

Wood is increasingly favored in construction for its high strength-to-weight ratio, renewability, and positive environmental impact. However, natural defects and size limitations inherent to wood necessitate the production of engineered wood products like glued laminated timber (glulam). Despite these advancements, moisture sensitivity remains a significant challenge in timber structures. Evaluation of 245 large-span timber structures revealed that moisture content variation contributes to 46% of structural damage causes (Dietsch et al. 2015).

To address these challenges, finite element method serves as a powerful tool for simulating moisture-induced stresses and assessing the response of wood products in diverse environmental conditions. Moisture content variation impacts wood in numerous ways. First, orthotropic hydro-expansion due to moisture changes can cause shape instability during technical drying and induce shrinkage stresses throughout both the drying process and the service life of timber structures (Ormarsson et al. 1998; Florisson et al. 2019; Brandstätter et al. 2023; Fortino et al. 2019). Additionally, moisture variation triggers mechano-sorptive creep and alters material parameters such as stiffness (Hassani 2015). An overview of the development of multi-field analyses that consider both hygroscopic and mechanical aspects of wood can be found in Yu et al. (2022 and Florisson and Gamstedt (2023). The constitutive model has been continuously improved and customized, aiming to cover diffusivity, hydro-expansion, elasticity, viscoelastic, mechano-sorption and damage/failure across different wood species.

However, works studying the growth-ring lay-up effect in glulam remain limited. According to the DIC (digital image correlation) measurements by Lee et al. (2019), the moisture-induced strain in glulam along the width direction is found to be dependent on the characteristics of all layers due to the effect of adjacent laminas along the glue line. Autengruber et al. (2021) also revealed how different pith locations can lead to varying shrinkage crack patterns in single boards. Brandstätter et al. (2023) further investigated shrinkage cracks in glulam cross-section under different moisture drying conditions using the XFEM method. This research (Brandstätter et al. 2023), as well as many other works (Jönsson and Thelandersson 2003; Zhou et al. 2010; Ormarsson and Gíslason 2016) on glulam, is restricted to only one specific lay-up, and the generalizability of their findings to different lay-up types is not discussed. The major challenge in studying the growth-ring effect on glulam lies in the difficulty of covering the infinite possibilities of the lamina lay-up options. Franke et al. (2016), as well as Aicher and Dill-Langer (2005), conducted numerical studies using several lay-up cases and confirmed the significant influence of the cross-section lay-up on the stress distributions and their maximum values. The attempt to cover the large number of lay-up possibilities can be found in the stochastic study by Yu et al. (2023), where a Monte Carlo analysis, taking the pith-location in different layers as input uncertainty, is conducted. A stress concentration factor of up to 1.56 was identified in curved glulam beams caused by bending loads.

In this work, to determine the growth-ring effect on moisture-induced stress, a Monte Carlo analysis following the approach in Yu et al. (2023) is first conducted in sections “Material and method” and “Results and discussion”. The analysis identified the major influence of the growth-ring of the target layer and the minor influence from the neighboring layers. These findings then facilitate two levels of simplification methods in section “Development of simplification methods” to analyze moisture-induced stress more efficiently. The first level aims to accelerate numerical simulations for more complex analyses, while the second level employs stronger assumptions to analytically estimate shrinkage stress for different pith types, moisture conditions, and wood species. In section “Application”, using these two simplification methods, the damage patterns of different board types are presented, along with a fast way to identify critical moisture variation magnitudes and preferable board types.

Material and method

Finite element model

The numerical model is built using Abaqus. Sequentially coupled thermal-mechanical models are adopted. In the thermal model, according to the mathematical analogy between heat transfer and moisture diffusion (Fortino et al. 2009), the transient moisture field can be computed. The computed transient moisture field is then taken as field input for the mechanical model where the moisture induced stresses are simulated.

This study will conduct Monte Carlo simulations across four different wood species, involving a large number of parameters and significant variability. Therefore, the selection of an appropriate constitutive material model is critical and must satisfy two key criteria: (1) demonstrated capability to capture the moisture transfer and elastic-damage behavior of wood, and (2) availability of relevant parameters in the literature. Accordingly, the constitutive models for heat transfer and mechanical analysis are adopted from Yu et al. (2022) and Seeber et al. (2024). The principal equations used are outlined below.The values of the involved parameters for different wood species are listed in Tables 1, 2 and 3.

Moisture transfer part

1. Constitutive equation:

$$\rho \frac{\partial u}{\partial t} = \mathbf{f} = \rho \nabla (\mathbf{D} \nabla u) \tag{1}$$

   where ρ, u, $\mathbf{f}$, $\mathbf{D}$, and t are the density of the material, the moisture content, the flux vector, the diffusivity tensor, and time, respectively.
2. Balance equation:

$$\int_V \mathbf{f}\, dV = \int_S J\, dS \tag{2}$$

   where V, S, and J are the volume of the material, the surface area, and the moisture flux through the surface, respectively.
3. Boundary condition:

$$J = -\rho S_u (u - u_{EMC}) \tag{3}$$

   where S_u and u_{EMC} are the surface emission coefficient and the equilibrium moisture content, respectively.

Mechanical part

1. Elasticity:

$$\frac{\partial \boldsymbol{\epsilon}^e}{\partial t} = \frac{\partial \boldsymbol{C}^{e-1}}{\partial t} \boldsymbol{\sigma} + \boldsymbol{C}^{e-1} \frac{\partial \boldsymbol{\sigma}}{\partial t} \tag{4}$$

   where $\boldsymbol{\epsilon}^e$, $\boldsymbol{C}^e$, and $\boldsymbol{\sigma}$ are the elastic strain, the elastic stiffness matrix, and the stress tensor, respectively.
2. Hydro-expansion:

$$\frac{\partial \boldsymbol{\epsilon}^{\boldsymbol{u}}}{\partial t} = \boldsymbol{\alpha}_{\boldsymbol{u}} \frac{\partial u}{\partial t} \tag{5}$$

Table 1 Material parameters of different wood species from the literature (Hassani et al. 2015; Pěnčík 2015; Qiu 2015)

Species	E_L (e4 MPa)	E_R (e2 MPa)	E_T (e2 MPa)	ν_{LR} (−)	ν_{LT} (−)	ν_{TR} (−)	G_{LR} (e2 MPa)	G_{LT} (e2 MPa)	G_{TR} (e2 MPa)
Spruce (Hassani et al. 2015)	1.2	8.2	4.2	0.41	0.54	0.34	6.5	7.6	0.42
Beech (Hassani et al. 2015)	1.4	19	6.1	0.28	0.23	0.28	13	8.9	4.9
Pine (Pěnčík 2015)	1.4	7.0	5.5	0.03	0.04	0.29	12	8.0	5.0
Larch (Qiu 2015)	1.7	12	11	0.37	0.49	0.49	6.2	3.4	0.55

Considering the measuring accuracy, all numbers are rounded to 2 scientific digits; Poisson's ratios (ν_{RL}, ν_{TL}, ν_{RT}) are calculated from the original literature assuming $\frac{\nu_{ij}}{E_i} = \frac{\nu_{ji}}{E_j}$; for Beech and Spruce, moisture dependent data is used according to Hassani et al. (2015), the value listed here are at moisture content u = 0.12

where $\boldsymbol{\epsilon}^{\boldsymbol{u}}$ and $\boldsymbol{\alpha}_{\boldsymbol{u}}$ are the hydro-expansion strain and the hydro-expansion coefficient, respectively.

3. SDM (Separate Damage Mode) damage initiation criteria:

$$F_{t/v,i} = \frac{|\sigma_i|}{f_i} \qquad i = R, T, RT \tag{6}$$

where $F_{t/v,i}$, σ_i, and f_i are the damage initiation criterion, the stress, the strength in direction i, respectively.

4. Damage propagation:

$$d_i = 1 - \frac{1}{F_{t/v,i}} \left[1 - \alpha + \alpha \exp\left(-\beta(F_{t/v,i} - 1)\right) \right] \tag{7}$$

where d_i is the damage variable, $\alpha = 0.99$ and $\beta = 0.1$ according to Seeber et al. (2024).

Figure 1 shows the overview of the finite element model. The simulated glulam beams consist of n ($n = 5, 9, 11, 15, 19$) layers of board with a cross-section of $40\,\mathrm{mm} \times 200\,\mathrm{mm}$. Each board is assigned a cylindrical coordinate system, characterized by a pith coordinate (y, z) using the center point as the origin (see Fig. 3). Although 2D model would be sufficient for the analysis in this work, the 3D eight-node brick element (C3D8) is chosen here to facilitate future extensions such as inclusion of slope of grain or analysis of curved glulam beams. In longitudinal direction, the model dimension was chosen with one element (4 mm) to model plain-strain conditions. Hence, after convergence analysis, each layer is discretized into 500 elements.

The initial moisture content, $u_{\mathrm{EMC}}^{\mathrm{initial}}$, is assigned to the entire model. Film conditions are then applied to the four side surfaces of the glulam, with a sink value of $u_{\mathrm{EMC}}^{\mathrm{initial}} - \Delta u_{\mathrm{EMC}}$. Figure 2 shows the equilibrium moisture content (u_{EMC}), calculated using the isotherms equation (Eq. 8) (Avramidis 1989). The temperature and relative

Table 2 Hydro-expansion coefficient (Hassani et al. 2015; Fortino et al. 2009; Qiu 2015)

Species	α_R	α_T	α_L
Spruce (Fortino et al. 2009)	0.17	0.33	0.005
Beech (Hassani et al. 2015)	0.19	0.46	0.011
Pine (Fortino et al. 2009)	0.13	0.27	0.005
Larch (Qiu 2015)	0.13	0.27	0.005

Table 3 Strength parameters for beech, pine, and larch (Seeber et al. 2024; Pěnčík 2015; Qiu 2015)

Species	$f_{t,R}$ (MPa)	$f_{t,T}$ (MPa)	$f_{v,RT}$ (MPa)
Beech (Seeber et al. 2024)	18	7	7
Pine (Pěnčík 2015)	5.4	4.9	2.3
Larch (Qiu 2015)	2.3	2.3	0.5

For larch, Qiu (2015) provided strength perpendicular to grain $f_{t,90}$ = 2.31 MPa, which is adopted here for both $f_{t,R}$ and $f_{t,T}$

humidity data are sourced from the Deutscher Wetterdienst for Munich (Germany), recorded over 365 days starting from February 2023 (Fig. 2). As a result, u_{EMC} fluctuates between 0.04 and 0.28. Since $u_{\mathrm{EMC}}^{\mathrm{initial}}$ under standard storage conditions (T = 20°C, RH = 65%) equals 0.12, the Δu_{EMC} (for the drying scenario only) is selected to range between 0.01 and 0.07.

$$u_{EMC} = 0.01 \cdot \left(- \frac{(T + 273.15) \cdot \ln(1 - \mathrm{RH})}{0.13 \cdot \left(1 - \frac{(T+273.15)}{647.1}\right)^{-6.46}} \right)^{\frac{1}{110 \cdot (T+273.15)^{-0.75}}} \tag{8}$$

Monte Carlo simulation

To analyze the growth-ring effect on moisture-induced stress, two test sets are conducted:

- *Test Set I* 30 subsets are conducted for Test Set I. In each subset, the pith location of the middle layer are controlled to be the same. The 30 subsets corresponds to 30 types of middle layer, where the pith location are selected from a uniform grid as shown in Fig. 3, where $y = -20, -60, -100, -140, -180$ mm and $z = -200, -150, -100, -50, -25, 0$ mm. For each subset, 50 simulations are conducted. In each simulation, the pith location of all other layers varies in the way that the y and zcoordinate of the pith are uniform random variables in the range of $y \in [-200, 0]$ mm and $z \in [-200, 200]$ mm.
- *Test Set II* For each simulation, each board layer is assigned a different random pith location. 300 simulations are conducted.

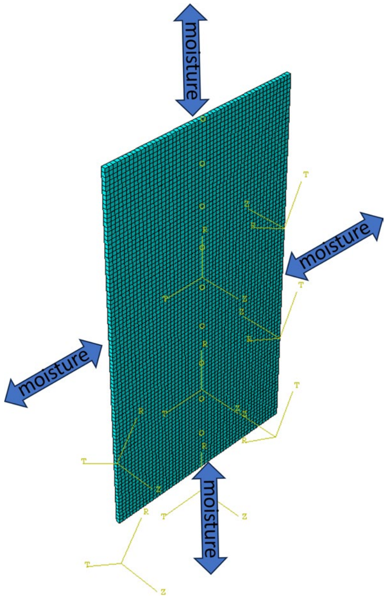

Fig. 1 Finite element model

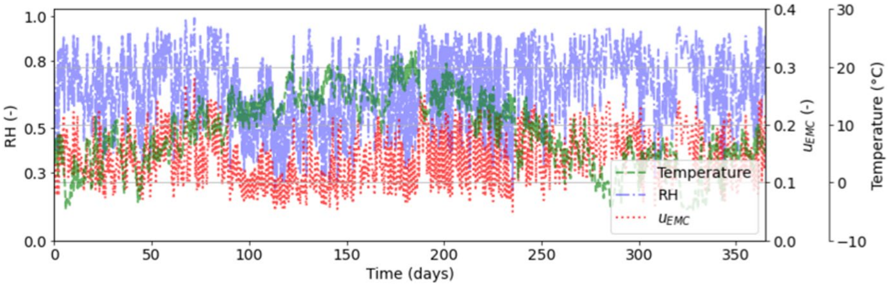

Fig. 2 Environment data

Moreover, both Test Sets are conducted for different wood species in Table 1, for glulam that is composed of different number of layers n (n = 5, 9, 11, 15, 19), as well as for different humidity conditions (Δu_{EMC} = 0.01, 0.03, 0.05, 0.07).

Results and discussion

Overview of stress development

Figure 4 shows the spatial moisture and stress distribution in a simulation example at day 33 after placing into dry condition. The model parameters are:

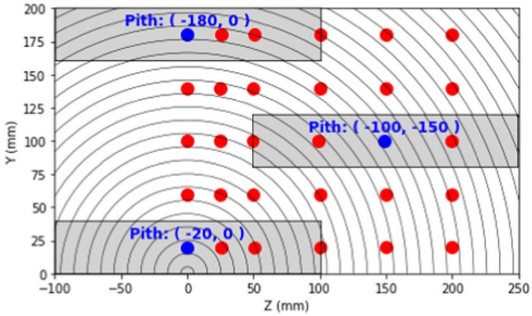

Fig. 3 The pith coordinates (y,z) are negative in the above examples as the individual board centers are taken as the origins. Pith location grid with 3 board example

- number of layers: n = 11;
- controlled pith of the middle layer: (y,z) = (− 60, − 150) mm;
- humidity condition: $\Delta u_{EMC} = 0.01$.

It can be observed that as moisture diffuses out from the four surfaces, the highest tensile stresses predominantly develop in the surface regions.In contrast, in the case of moisture uptake, tensile stresses would form in the central region, with a lower magnitude compared to the stress concentration in the surface region observed in the drying cases. Moreover, the varying pith locations of each layer result in differences in the distribution of both moisture content and stresses, with particularly notable variations in stress distribution, highlighting the importance of analysing the growth-ring effect.

Figure 5 shows the moisture (Δu) and tangential stress (σ_T) development at the surface region of the middle layer over 90 days. For all locations and moisture conditions (Δu_{EMC}) studied here, the evolution of stress closely follows the pattern of moisture content change (Δu). However, while Δu continues to increase at a decreasing rate, σ_T begins to decrease after reaching a maximum. This occurs because the moisture content in the center region also decreases over time, albeit with a delay compared to the surface region. This delay results in a smaller moisture difference between the surface and center regions, leading to a decrease in the tensile stress in the surface region. Additionally, locations closer to the surface exhibit higher maximum stress and a shorter time to reach that maximum.

Results of Test Set I

Figure 6 depicts the stress distribution within the same middle layer, considering various pith locations of the neighboring layers. Despite minor variations, the stress distribution in the middle layer shows remarkable similarity across different configurations of the neighboring layers.

To provide a quantitative analysis, Fig. 7 presents the statistical distribution (obtained from 50 simulations of each type of middle layer) of tangential stress at four board corners (marked with x) for three exemplary types of the middle layer: with pith locations at (− 20, 0) mm, (− 40, − 50) mm, and (− 60, − 150) mm,

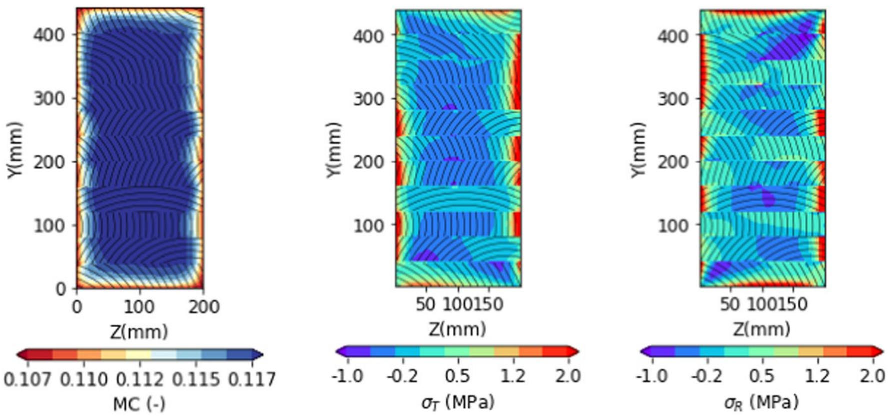

Fig. 4 Moisture and stress distribution at 33rd day after placing in dry condition of $\Delta u_{EMC} = 0.01$

respectively. The average stress across different locations of these three types ranges from 0.79 to 1.69 MPa. In contrast, the stress variation within a specific corner of a particular middle layer is confined to a range smaller than 0.3 MPa.

A normal distribution is employed to fit the data, and the standard deviations consistently measure below 0.07 MPa. This observation suggests that the influence of the layups of neighboring layers on stress distribution is limited.

Furthermore, it is observed that points sharing the same material rotational angle θ exhibit consistent average stresses, regardless of the middle layer type, such as Point C of the first and second example in Fig. 7. To validate this observation, stress values are plotted against the rotational angle for all simulations across all 30 types of middle layers in Fig. 8.

Based on the above analysis, the following conclusions can be drawn regarding the stresses in the middle layer:

- Observation I: stresses are minimally affected by the layups of neighboring layers.
- Observation II: stresses exhibit a strong correlation with the rotational angle of the material.

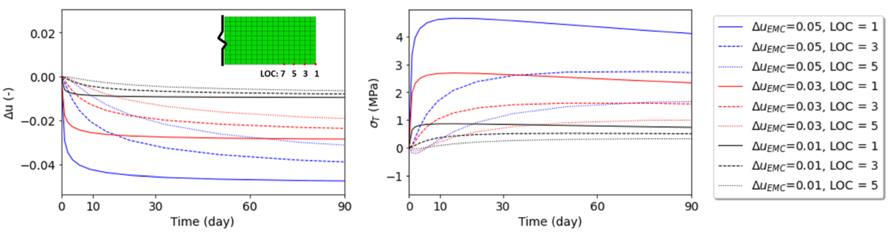

Fig. 5 Moisture and stress development at surface region (LOC i represents the outermost node of the i^{th} element from the surface)

Results of Test Set II

In this test set, the goal is to validate the aforementioned features across various wood layers, times, locations, and wood species.

Figure 9 displays the tangential stress values versus rotational angles in different layers of a 9-layer glulam beam. It can be seen that, except for the top and bottom layers, all layers exhibit an almost identical relation between stress and rotational angle. The top and bottom layers, however, show two distinct types of curves. This is due to the boundary conditions at locations C and D for the top layer and at locations A and B for the bottom layer, which are essentially free.

As shown in Fig. 10, one day after placing the beam in dry conditions, tangential stress is only evident at location Loc = 1 (location definition is shown in Fig. 5) and remains at 0 MPa at all other locations. After one month, stress variations start to appear at all locations but are smaller further away from the surface. This can be explained by moisture penetrating deeper into the beam over time. At each time point, the further the distance from the surface, the smaller the magnitude of the moisture content change.

It is observed that the variation of stress at the same angle becomes larger over time. At three years after placing the beam in dry conditions, the correlation is almost not noticeable.

Hence, it can be concluded that the aforementioned features found in *Test Set I* are valid for:

- all board layers except for the top and bottom;
- different locations where the distance to the side surface is between (0, Y) mm.
- a limited time period between (0, X) days.
- as observed in Monte Carlo simulations, for a board dimension of 40 mm × 200 mm, Y is no less than 30 mm and X is no less than 30 days.

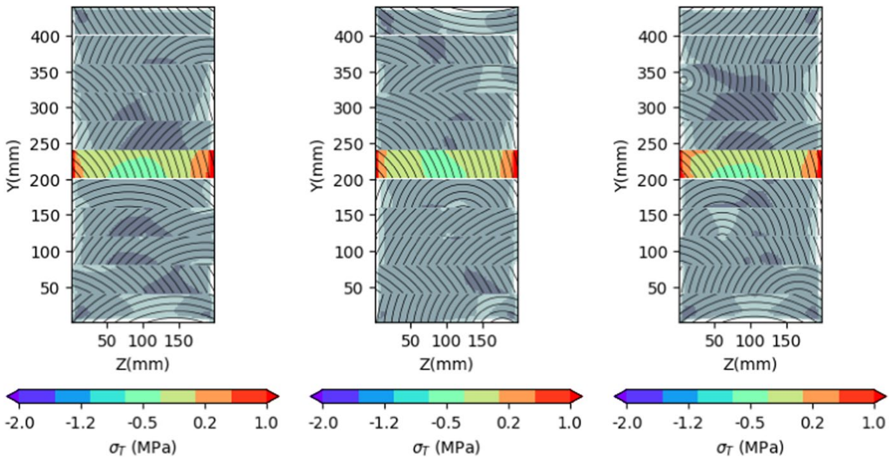

Fig. 6 Tangential stress of the same middle layer with different layups to other layers: $\Delta u_{EMC} = 0.01$, Pith of middle layer = (− 60, −150) mm, Time = 1st day

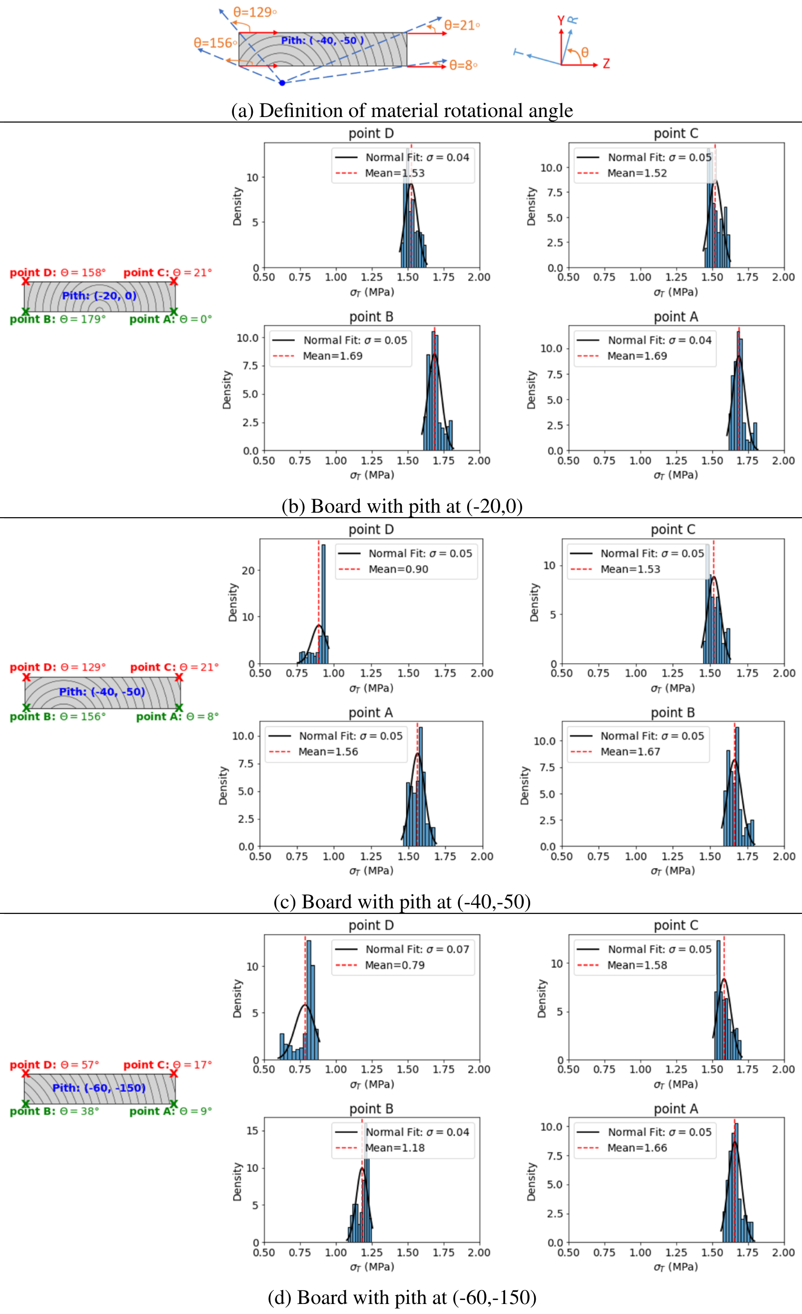

Fig. 7 Statistic distribution of tangential stress at the corners of the middle layer (Δu_{EMC} = 0.01, Time = 1st day)

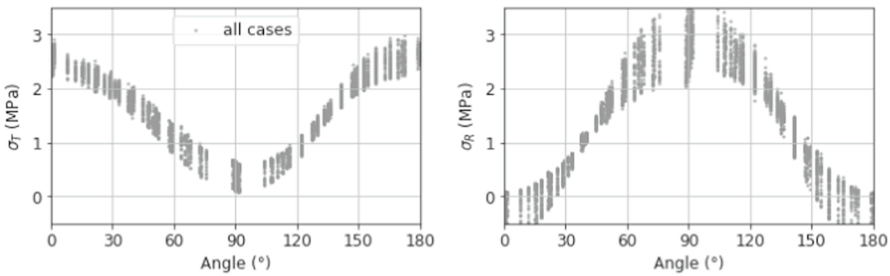

Fig. 8 Stress vs rotational angle: $\Delta u_{EMC} = 0.01$, Time = 1st day, LOC = 1 (LOC definition see Fig. 5)

Development of simplification methods

First level of simplification

Based on the Observation I from *Test Set I* and *Test Set II*, where the stress in most board layers is only slightly influenced by the neighboring layers, it is logical to assume that the multi-layered glulam problem can be simplified to a single-board problem. This simplification is depicted in Fig. 11, where the influence of the neighboring layers is abstracted into a rotational boundary condition.

To validate this assumption and to understand why the influence of neighboring layers is minimal, it is crucial to comprehend the underlying mechanisms of stress development.

From the spatial distribution of moisture content and stress shown in Fig. 4, it can be seen that after one month, only a very limited depth is influenced by the humidity change due to the slow diffusion process in wood. Consequently, most of the central region exhibits almost zero stress, while only the surface region experiences high tensile stress due to the shrinkage in this area. Based on this observation, the central region can be considered a rigid body, maintaining almost constant moisture content and stress over a certain time range. Therefore, the problem can be represented using the sketch shown in Fig. 12. The steps in Fig. 12 and the corresponding moisture and mechanical states are:

- *Initial State*
  - *Moisture state* $u_P^{\text{initial}} = u_{\text{EMC}}^{\text{initial}}$ for any point P in Center Region and Surface Region.
  - *Strain state* Zero deformation in Center Region and Surface Region.
  - *Stress state* Zero stress in Center Region and Surface Region.
- *Virtual Free-Shrinkage State*
  - *This is a virtual state with assumed free boundary condition* Surface Region can shrink freely without any restriction from the Center Region or neighboring layers (i.e., no connection between the Surface Region and the Center Region, and no connection between layers).

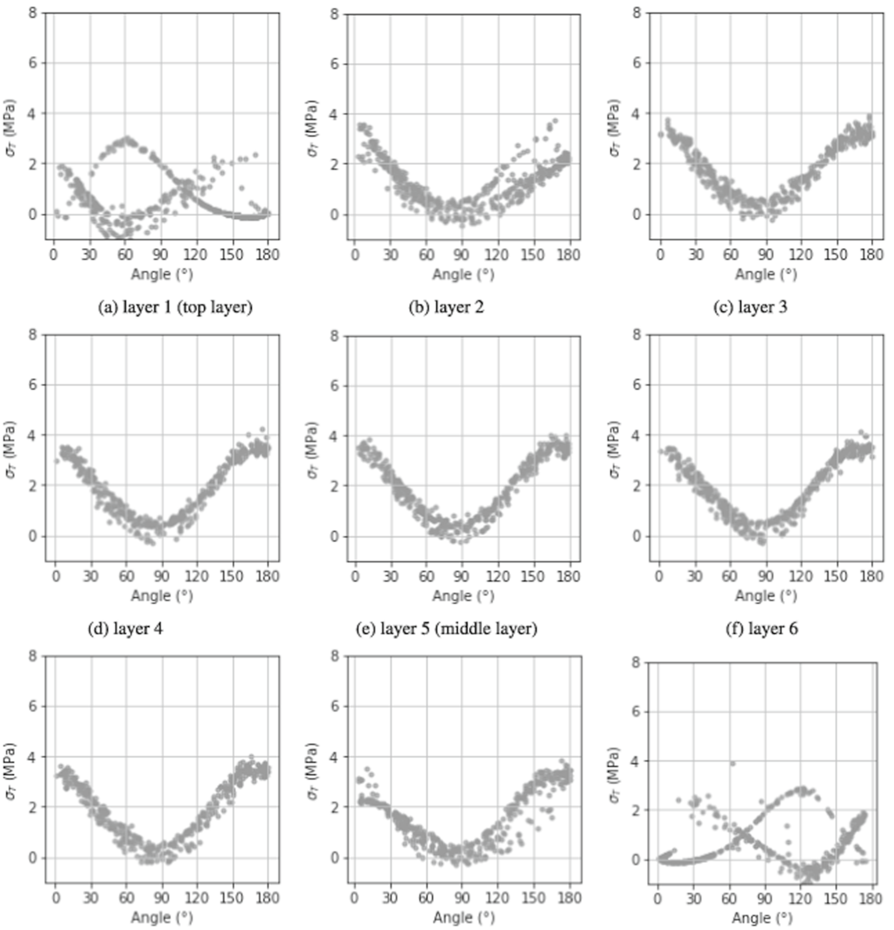

(a) layer 1 (top layer) (b) layer 2 (c) layer 3
(d) layer 4 (e) layer 5 (middle layer) (f) layer 6
(f) layer 7 (g) layer 8 (h) layer 9 (bottom layer)

Fig. 9 Stress vs rotational angle at different layers: species = Beech, $\Delta u_{EMC} = 0.03$, Time = 33[rd] day, LOC = 3

- *Moisture state* $u_P^{\text{free}} \in [u_{\text{EMC}}^{\text{initial}} - \Delta u_{\text{EMC}}, u_{\text{EMC}}^{\text{initial}}]$ point P in the Surface Region, and $u_{\text{Center}}^{\text{free}} \approx u_{\text{EMC}}^{\text{initial}}$ for the Center Region.
- *Strain state* Free shrinkage for the Surface Region according to u_P^{free}; approximate zero deformation for the Center Region.
- *Stress state* Almost zero stress in all regions due to the free shrinkage.

- *End State*
  - *Boundary condition* Deformation of the Surface Region is restricted by the Center Region and the Surface Regions of two neighboring layers.
  - *Moisture state* $u_P^{\text{end}} \in [u_{\text{EMC}}^{\text{initial}} - \Delta u_{\text{EMC}}, u_{\text{EMC}}^{\text{initial}}]$ for the Surface Region, and $u_{\text{Center}}^{\text{end}} \approx u_{\text{EMC}}^{\text{initial}}$ for the Center Region.

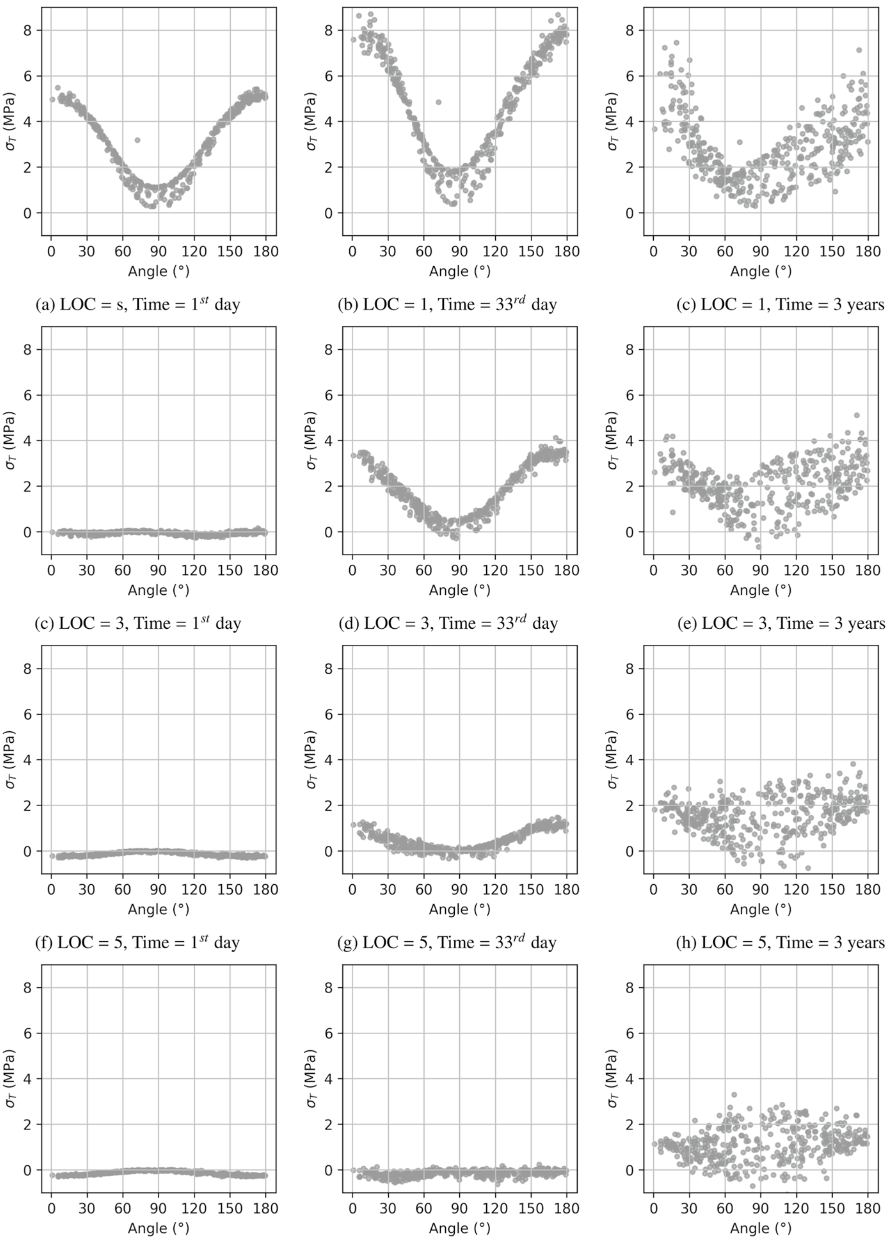

(a) LOC = s, Time = 1^{st} day
(b) LOC = 1, Time = 33^{rd} day
(c) LOC = 1, Time = 3 years
(c) LOC = 3, Time = 1^{st} day
(d) LOC = 3, Time = 33^{rd} day
(e) LOC = 3, Time = 3 years
(f) LOC = 5, Time = 1^{st} day
(g) LOC = 5, Time = 33^{rd} day
(h) LOC = 5, Time = 3 years
(i) LOC = 7, Time = 1^{st} day
(j) LOC = 7, Time = 33^{rd} day
(k) LOC = 7, Time = 3 years

Fig. 10 Stress vs rotational angle at different locations and time points: species = Beech, $\Delta u_{EMC} = 0.03$

– *Strain state* Approximate zero deformation for the Center Region. Deformation in the Y direction of the Surface Region recovers to approximate

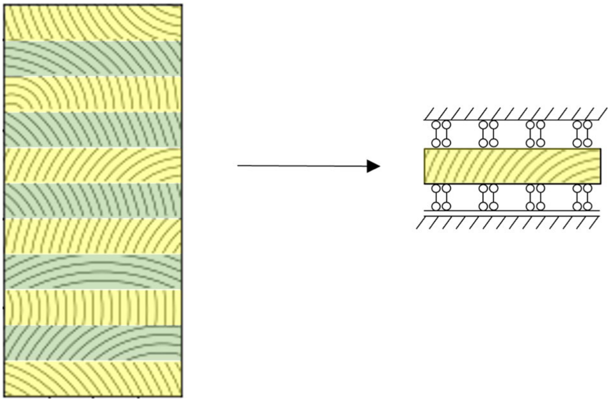

Fig. 11 First level of simplification

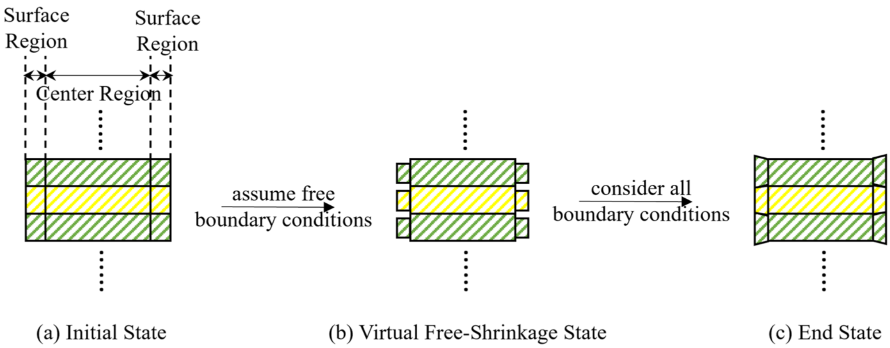

Fig. 12 Sketch of the deformation at three states

the same state as the Center Region, with slight differences due to variations in global stiffness between layers.

– *Stress state* Approximate zero stress for the Center Region; tensile stress for the Surface Region due to the strain difference between the End State and the Free-Shrinkage State.

From the above analysis, it is clear that stress arises because that the surface region is restricted in the End State, in comparison to the Virtual Free-Shrinkage State. This restriction is caused by the two neighboring layers. Moreover, how strong the restriction is dependent on the local stiffness of the neighboring layer at the surface region, which can be determined by the local material direction.

If the material direction of the analyzed layer aligns with its two neighboring layers, then the surface region at the end state should return to the same level as the initial state, resembling the boundary condition depicted in Fig. 11. However, due to differences in the pith location between layers, the returned level is not exactly the same as the initial state, which explains the fluctuation of stress within the same layer as observed in Fig. 7 in *Test Set I*.

Nonetheless, because the surface region has a shallow depth, the center region can be considered almost as a rigid body. This means the recovered level of the surface region is nearly equivalent to the initial state, and the influence of the neighboring layers is small compared to the influence of the center region, explain the Observation I in *Test Set I*.

Consequently, Fig. 13 presents the stress-angle relationship as simulated by both the full glulam analysis (real case) and the first level of simplification method for different species. The strong quantitative agreement between these results validates the simplification method across different locations and various wood species.

To summarize, the first level of simplification relies on the observation that varying the pith location of neighboring layers has minimal impact on the stress levels of the analyzed layer. Therefore, the primary assumption and limitation of this simplification is the disregard of this influence. Additional, such simplification is not valid for the most top and bottom layer.

The main advantage is that it reduces the multi-layer problem to a single-layer problem, making it easier to perform more complex analyses that requires sophisticated material models and higher computational cost. An example is the damage evolution analysis that will be shown in the next chapter.

Second level of simplification

Although the first level of simplification significantly reduces computational costs, certain observations from the Monte Carlo simulation (as shown in Fig. 13) remain unexplained:

- Why does the stress in the surface region exhibit such a strong non-linear correlation with the rotation angle?
- Why does this correlation vary between different species?
- What is the primary material parameter that determines the maximum stress?

If we can derive an analytical equation to explain this non-linear correlation, we could generate the correlation curve and estimate the maximum stress for different species in a matter of seconds, instead of conducting extensive numerical simulations for various types of boards and species.

To achieve this, the problem needs to be further simplified to the single-element level, as shown in Fig. 14. Building upon the problem abstraction outlined in Fig. 12 and the success of simplifying the influence of the neighboring layers to rotational boundary conditions, it is logical to assume that the influence of the center region can similarly be characterized by a fixed boundary condition on one side.

Neglecting the effect in the longitudinal direction, the stiffness matrix ($\boldsymbol{C}$) and rotational matrices ($\boldsymbol{T}^{\epsilon}, \boldsymbol{T}^{\sigma}$) are given by:

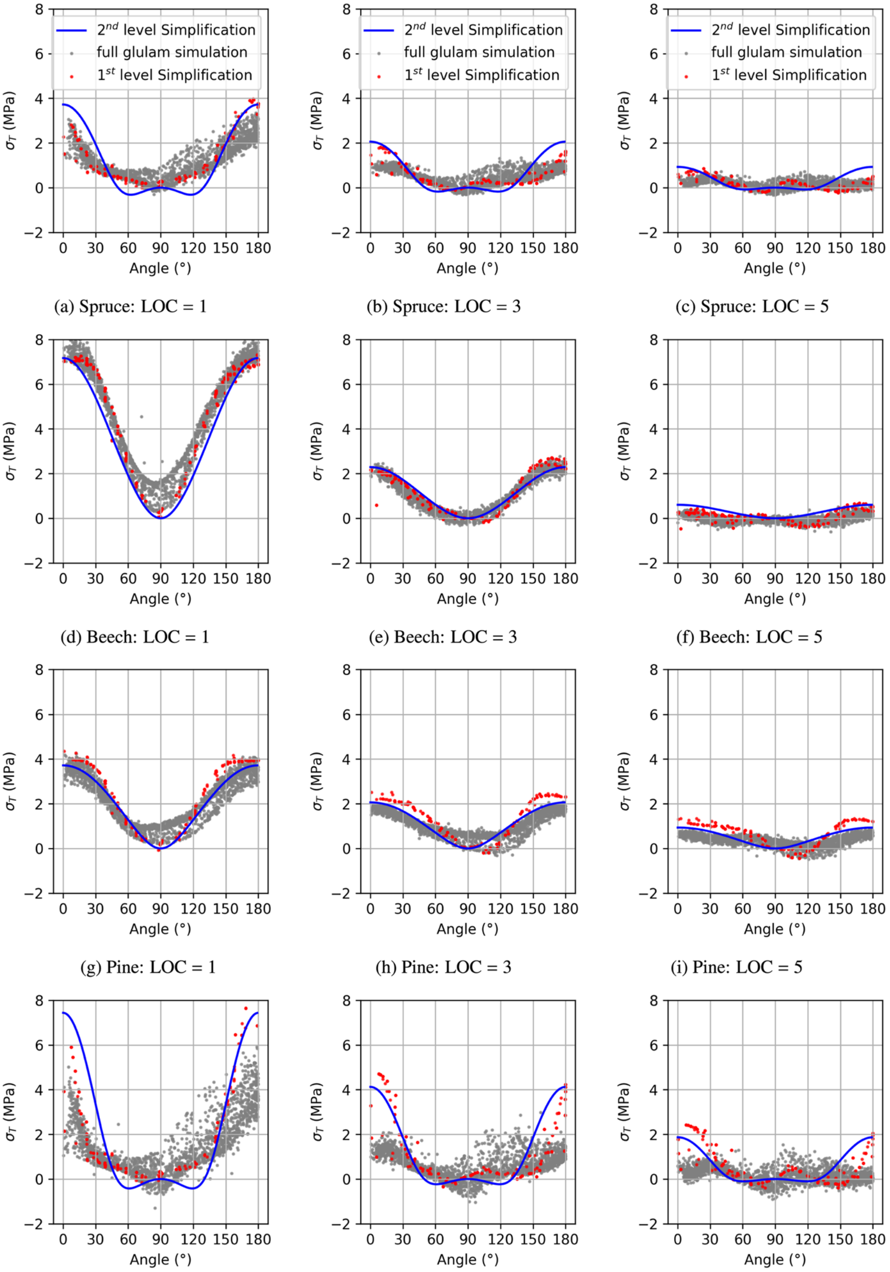

(a) Spruce: LOC = 1
(b) Spruce: LOC = 3
(c) Spruce: LOC = 5
(d) Beech: LOC = 1
(e) Beech: LOC = 3
(f) Beech: LOC = 5
(g) Pine: LOC = 1
(h) Pine: LOC = 3
(i) Pine: LOC = 5
(j) Larch: LOC = 1
(k) Larch: LOC = 3
(l) Larch: LOC = 5

Fig. 13 Stress versus rotational angle of different species at different locations (from inner 5 layers of 9-layer glulam): $\Delta u_{EMC} = 0.03$, Time $= 14^{\text{th}}$ day

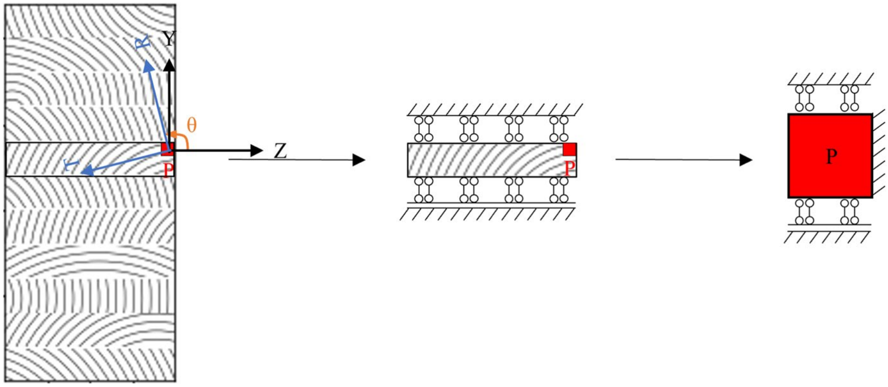

Fig. 14 Second level of simplification

$$\boldsymbol{C} = \begin{bmatrix} \frac{1}{E_T} & \frac{\nu_{RT}}{E_R} & 0 \\ \frac{\nu_{TR}}{E_T} & \frac{1}{E_R} & 0 \\ 0 & 0 & \frac{G_{RT}(1-\nu_{RT}\nu_{TR})}{E_R E_T} \end{bmatrix} \frac{E_R E_T}{1-\nu_{RT}\nu_{TR}} \tag{9}$$

$$\boldsymbol{T}^{\epsilon} = \begin{bmatrix} cos_\theta^2 & sin_\theta^2 & cos_\theta sin_\theta \\ sin_\theta^2 & cos_\theta^2 & -cos_\theta sin_\theta \\ -2cos_\theta sin_\theta & 2cos_\theta sin_\theta & cos_\theta^2 - sin_\theta^2 \end{bmatrix} \tag{10}$$

$$\boldsymbol{T}^{\sigma} = \begin{bmatrix} cos_\theta^2 & sin_\theta^2 & 2cos_\theta sin_\theta \\ sin_\theta^2 & cos_\theta^2 & -2cos_\theta sin_\theta \\ -cos_\theta sin_\theta & cos_\theta sin_\theta & cos_\theta^2 - sin_\theta^2 \end{bmatrix} \tag{11}$$

If the element P can shrink freely (as shown in Fig. 12 Free Shrinkage State), the free shrinkage strain in the local ($\boldsymbol{\epsilon}_{P,local}^{free}$) and global coordinate system ($\boldsymbol{\epsilon}_{P,global}^{free}$) are:

$$\boldsymbol{\epsilon}_{P,local}^{free} = \begin{bmatrix} \alpha_R \\ \alpha_T \\ 0 \end{bmatrix} (u_P^{free} - u_P^{initial}) = \begin{bmatrix} \alpha_R \\ \alpha_T \\ 0 \end{bmatrix} (u_P^{end} - u_P^{initial}) \tag{12}$$

$$\boldsymbol{\epsilon}_{P,global}^{free} = T^{\epsilon} \epsilon_{P,local}^{free} = \begin{bmatrix} cos_\theta^2 \alpha_R + sin_\theta^2 \alpha_T \\ sin_\theta^2 \alpha_R + cos_\theta^2 \alpha_T \\ -2cos_\theta sin_\theta (\alpha_R - \alpha_T) \end{bmatrix} (u_P^{end} - u_P^{initial}) \tag{13}$$

where α_R and α_T are the hydro-expansion coefficients. u_P^{end}, u_P^{free}, $u_P^{initial}$ represent the moisture content of element P at the End, Virtual Free-Shrinkage, and Initial State, respectively.

Hence, the strain changes $\Delta\epsilon_{P,global}$ between End State and Free Shrinkage State can be calculated as:

$$\Delta\boldsymbol{\epsilon}_{P,global}=\begin{bmatrix}\Delta\epsilon_{P_Z}\\ \Delta\epsilon_{P_Y}\\ \Delta\gamma_{P_{ZY}}\end{bmatrix}=\boldsymbol{\epsilon}^{end}_{P,global}-\boldsymbol{\epsilon}^{free}_{P,global}$$
$$=\begin{bmatrix}\epsilon^{end}_{P_Z}\\ \epsilon^{end}_{P_Y}\\ \gamma^{end}_{P_{ZY}}\end{bmatrix}-\epsilon^{free}_{P,global}=\begin{bmatrix}\epsilon^{end}_{P_Z}-(cos^2_\theta\alpha_R+sin^2_\theta\alpha_T)(u^{end}_P-u^{initial}_P)\\ \epsilon^{end}_{P_Y}-(sin^2_\theta\alpha_R+cos^2_\theta\alpha_T)(u^{end}_P-u^{initial}_P)\\ \Delta\gamma_{P_{ZY}}\end{bmatrix} \tag{14}$$

and the corresponding final stress $\boldsymbol{\sigma}^{end}_{P,global}$ can be calculated as:

$$\boldsymbol{\sigma}^{end}_{P,global}=\begin{bmatrix}\sigma^{end}_{P_Z}\\ \sigma^{end}_{P_Y}\\ \tau^{end}_{P_{ZY}}\end{bmatrix}=\boldsymbol{T}^{\sigma}\boldsymbol{C}\boldsymbol{T}^{\epsilon-1}\Delta\boldsymbol{\epsilon}_{P,global}=\begin{bmatrix}C'_{11} & C'_{12} & C'_{13}\\ C'_{21} & C'_{22} & C'_{23}\\ C'_{31} & C'_{32} & C'_{33}\end{bmatrix}\begin{bmatrix}\Delta\epsilon_{P_Z}\\ \Delta\epsilon_{P_Y}\\ \Delta\gamma_{P_{ZY}}\end{bmatrix} \tag{15}$$

According to Fig. 14, the boundary conditions in this level of simplification indicate:

- the rotation strain in End and Virtual Free-Shrinkage remains the same:

$$\Delta\gamma_{P_{ZY}}=0 \tag{16}$$

- at the End State, the stress in Z direction is zero:

$$\sigma^{end}_{P_Z}=0 \tag{17}$$

- at the End State, element P will have the same strain in Y direction as the Center Region:

$$\epsilon^{end}_{P_Y}=\epsilon^{end}_{Center\ Y} \tag{18}$$

- additionally, assume the element in the Center Region next to element P to have the same rotational angle as element P, the strain at the End State in Y direction of center region ($\epsilon^{end}_{Center\ Y}$) becomes:

$$\epsilon^{end}_{Center\ Y}=(sin^2_\theta\alpha_R+cos^2_\theta\alpha_T)(u^{end}_{Center}-u^{initial}_{Center}) \tag{19}$$

Substituting Eqs. 16 and 17 into Eq. 15:

$$\Delta\epsilon_{P_Z}=-\frac{C'_{12}}{C'_{11}}\Delta\epsilon_{P_Y} \tag{20}$$

Substituting Eqs. 18 and 19 into Eq. 14:

$$\Delta\epsilon_{P_Y} = (sin^2_\theta \alpha_R + cos^2_\theta \alpha_T)(u^{end}_{Center} - u^{end}_P) \tag{21}$$

So far, all components of strain difference between End State and Virtual Free-Shrinkage State ($\Delta\boldsymbol{\epsilon}_{P,global}$) are solved:

$$\Delta\boldsymbol{\epsilon}_{P,global} = \begin{bmatrix} \Delta\epsilon_{P_Z} \\ \Delta\epsilon_{P_Y} \\ \Delta\gamma_{P_{ZY}} \end{bmatrix} = \begin{bmatrix} -\frac{C'_{12}}{C'_{11}} \\ 1 \\ 0 \end{bmatrix} (sin^2_\theta \alpha_R + cos^2_\theta \alpha_T)(u^{end}_{Center} - u^{end}_P) \tag{22}$$

Finally, the local stress at the End State ($\sigma^{end}_{P,local}$) can be easily calculated from $\Delta\epsilon_{P,global}$ as:

$$\boldsymbol{\sigma}^{end}_{P,local} = \begin{bmatrix} \sigma^{end}_{P_R} \\ \sigma^{end}_{P_T} \\ \tau^{end}_{P_{RT}} \end{bmatrix} = \boldsymbol{CT}^{\epsilon-1}\Delta\boldsymbol{\epsilon}_{P,global} = \begin{bmatrix} C''_{11} & C''_{12} & C''_{13} \\ C''_{21} & C''_{22} & C''_{23} \\ C''_{31} & C''_{32} & C''_{33} \end{bmatrix} \begin{bmatrix} \Delta\epsilon_{P_Z} \\ \Delta\epsilon_{P_Y} \\ \Delta\gamma_{P_{ZY}} \end{bmatrix} \tag{23}$$

which gives:

$$\sigma^{end}_{P_R} = \left(-\frac{C'_{12}}{C'_{11}}C''_{11} + C''_{12}\right)\Omega \tag{24}$$

$$\sigma^{end}_{P_T} = \left(-\frac{C'_{12}}{C'_{11}}C''_{21} + C''_{22}\right)\Omega \tag{25}$$

$$\tau^{end}_{P_{RT}} = \left(-\frac{C'_{12}}{C'_{11}}C''_{31} + C''_{32}\right)\Omega \tag{26}$$

$$\Omega = [sin^2_\theta(\alpha_R - \alpha_T) + \alpha_T](u^{end}_{Center} - u^{end}_P) \tag{27}$$

where C''_{ij} are the components of $\boldsymbol{CT}^{\epsilon-1}$.

The validation of the above solutions is presented in Fig. 13 for different locations and wood species. Moreover, it is important to note that both simplification methods have also been validated for various Δu_{EMC} conditions, different time (ranging from 1^{st} to 14^{th} day), and different stress components (σ_R, σ_T, τ_{RT}).

To summarize, the second level of simplification further abstracts the influence of the center region on Element P of the surface region as a fixed boundary condition, which is mathematically represented by Eqs. 16–19. Correspondingly, this method is valid only within the elastic range and during periods when moisture changes in the center region are minimal.

The major advantage is the clear elucidation of how stress is influenced by the rotational angle, stiffness, and hydro-expansion coefficients. This means that for any new wood species, a quick estimation of the moisture-induced stress level can be achieved without conducting numerical simulations. It also provides information such as the critical rotational angle, critical moisture range, and preferred board type, as will be demonstrated in the next chapter.

Application

Application of second level of simplifcation

Critical rotational angle

According to Eqs. 24 and 25, the stress at two extreme angles can be calculated:

when $\theta = 0°$:

$$\sigma_{P_R}^{end,0°} = 0 \tag{28}$$

$$\sigma_{P_T}^{end,0°} = E_T \alpha_T (u_{\mathrm{Center}}^{end} - u_P^{end}) \tag{29}$$

when $\theta = 90°$:

$$\sigma_{P_R}^{end,90°} = E_R \alpha_R (u_{\mathrm{Center}}^{end} - u_P^{end}) \tag{30}$$

$$\sigma_{P_T}^{end,90°} = 0 \tag{31}$$

$\sigma_{P_T}^{end,0°}$ and $\sigma_{P_R}^{end,90°}$ represent approximately the maximum tangential stress and maximum radial stress, respectively. Accordingly, Fig. 15 shows examples of boards that will exhibit the highest tangential/radial stress.

The first board type in Fig. 15, where the pith is located at (− 20 mm, 0 mm), is frequently considered a critical case in various studies (Brandstätter et al. 2023; Jönsson and Thelandersson 2003; Zhou et al. 2010). However, this assumption appears to lack sufficient justification. While this board type does represent the scenario with the highest tangential stress induced by moisture, it remains unclear if it corresponds to the earliest initiation of damage and how extensively the damage will develop. These issues will be addressed in the following section.

Critical moisture fluctuation range

Instead of the absolute stress value, a more meaningful parameter to check is the damage variable. According to the initiation criterion of Separated Damage Mode (Seeber et al. 2023):

$$F_R = \frac{\sigma_R}{f_R} \tag{32}$$

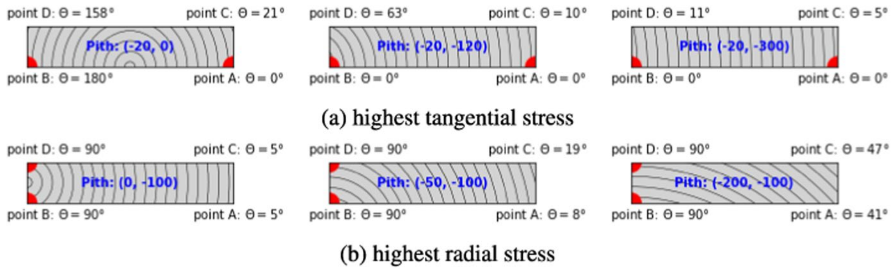

Fig. 15 Examples of boards with locations exhibiting highest stress (highlighted in red) (color figure online)

$$F_T = \frac{\sigma_T}{f_T} \tag{33}$$

The damage variable versus the rotational angle can be seen in Fig. 16, according to the parameters from Tables 1, 2 and 3.

Moreover, this method can also be adopted for different failure criteria. As an example, the multi-surface Tsai-Wu failure criteria is considered for spruce (Lukacevic et al. 2017) with the corresponding parameters shown in Table 4:

$$\begin{aligned} F_i = \\ & a_{LL,i}\sigma_L + a_{RR,i}\sigma_R + a_{TT,i}\sigma_T + \\ & b_{LLLL,i}\sigma_L^2 + b_{RRRR,i}\sigma_R^2 + b_{TTTT,i}\sigma_T^2 + \\ & 2b_{RRTT,i}\sigma_T\sigma_R + \\ & 4b_{LRLR,i}\tau_{LT}^2 + 4b_{RTRT,i}\tau_{RT}^2 + 4b_{TLTL,i}\tau_{TL}^2 \end{aligned} \tag{34}$$

It can be seen that for all species, the most critical damage variable occurs at angle around 0 degree. To understand the reason, by considering SDM:

$$F_R^{max} \approx F_R^{90^\circ} = \frac{E_R\alpha_R}{f_R}\Delta u \tag{35}$$

$$F_T^{max} \approx F_T^{0^\circ} = \frac{E_T\alpha_T}{f_T}\Delta u \tag{36}$$

where Δu is moisture fluctuation magnitude, and $\Delta u = (u_{\text{Center}}^{end} - u_P^{end})$.

Hence, for a given wood species, whether F_T^{max} is larger than F_R^{max}-and thus whether boards with a surface angle of 0° or 90° will exceed the damage criteria first-depends on the ratios $\frac{E_T\alpha_T}{f_T}$ and $\frac{E_R\alpha_R}{f_R}$. The assumption that the board types in Fig. 15a are most critical in terms of damage initiation holds true under the condition that $\frac{E_T\alpha_T}{f_T} > \frac{E_R\alpha_R}{f_R}$.

In addition, the critical moisture fluctuation range Δu_{critic} can be calculated using:

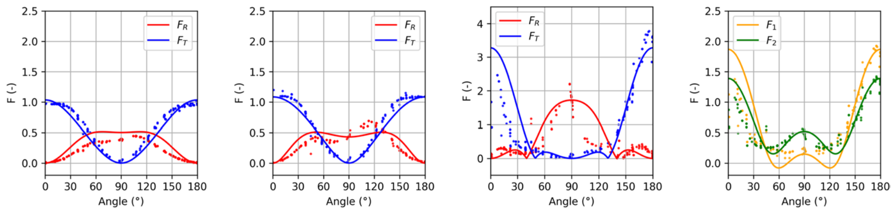

(a) Beech (b) Pine (c) Larch (d) Spruce

Fig. 16 Damage variable versus rotational angle ($\Delta u_{EMC} = 0.03$, LOC = 1, Time = 14[th] days)

Table 4 Damage parameter of spruce

Damage surface i	$a_{RR,i}$	$a_{TT,i}$	$b_{RRRR,i}$	$b_{TTTT,i}$	$b_{RTRT,i}$
$i = 1$	0.01173	0.47073	0.00713	0.00559	0.00048
$i = 2$	0.12170	0.34478	0.00405	0.00541	0.00138

$$\Delta u_{\text{critic}} = min(\Delta u|_{F_T^{max}=1}, \Delta u|_{F_R^{max}=1}) \approx min\left(\frac{f_T}{E_T\alpha_T}, \frac{f_R}{E_R\alpha_R}\right) \tag{37}$$

This value represents the change in moisture content that would lead to a violation of the damage criteria. If the moisture change remains below this threshold, the boards can be considered safe from shrinkage cracks. Consequently, Δu_{critic} for beech, pine, and larch are 2.5%, 2.4%, and 0.8%, respectively. Similarly, Δu_{critic} for spruce can be calculated according to the multi-surface Tsai-Wu criteria and the result is 1.4%.

Based on the adopted failure criteria, the glulam made from beech and pine are less prone to the shrinkage damage caused by moisture changes. Their Δu_{critic} values align well with the allowed fluctuation range of 2%, as suggested in an early research document by van der Velden and Kuipers (1976). However, spruce and larch are more susceptible to moisture-induced damage, indicating a need for stricter control on moisture fluctuation.

Preferred board type

Similar to Eq. 37, the critical moisture fluctuation range for all rotational angle can be inversely calculated, and the results for beech and spruce are shown in Fig. 17.

It can be seen that, for beech wood, by selecting boards with rotational angles between 30° and 150°, the critical moisture content for beech wood can be increased to 3.1%. For boards with rotational angles within the range of 45° to 135°, the critical moisture content can reach as high as 4.7%. Similarly, for spruce, the critical moisture contents are 2.7% and 4.5% for the rotational angle ranges of [30°, 150°] and [37°, 143°], respectively.

It is essential to point out that the conclusion is based on the simulation results, where the fluctuation range of Δu_{EMC} is below 0.07, and the elasticity of

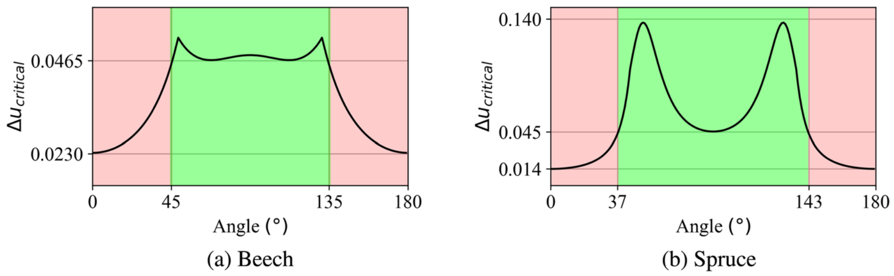

Fig. 17 Critical moisture content change

wood is considered to be moisture-independent. Additionaly, this work considers mainly the material rotational angle in the cross-section but not any fiber deviation. In reality, the hardwood species such as beech always presents stronger curvature in the longitudinal direction, posing challenging in controlling the cutting angles of the boards. For such species, the plausible way to estimate the moisture induced stress could be employing the first level of simplification and additionally implementing the fiber deviation information, which can be obtained through the scanning technique (Seeber et al. 2023; Huber et al. 2021; Lukacevic et al. 2019).

Application of first level of simplification: damage development

Based on Observation I from the Monte Carlo analysis, it can be inferred that the development of moisture-induced damage in a board within a glulam structure is primarily influenced by the material properties of the board itself, rather than the material properties of the neighboring layers. Hence, employing the first level of simplification, it streamlines the analysis process while still providing reliable insights into the damage evolution. Figure 18 shows the damage patterns of 25 types of boards with varying pith directions. In this simulation, the material used is beech, and the Δu_{EMC} is 0.03.

It can be seen that additional to the damage at the surface regions, significant damage can evolve inside the board. As the damage variable shown here is the tangential one, which is the most major damage for beech wood, it advances mainly in the radial direction. These simulated damage patterns qualitatively resemble the drying cracks observed in the real glulam beams in the work of Franke et al. (2015) and Bucur (2011). However, quantitative validation is still necessary, particularly concerning damage depth, the Δu_{EMC} level that activates damage, and other factors. Moreover, as the simulation is a sequentially-coupled moisture-mechanical analysis, the evolution of damage is assumed to have no influence on moisture diffusion in this study.

Nevertheless, examining the evolution of moisture content, stress, and damage parameters at different simulation increments, as depicted in Fig. 19, provides a possible explanation for the major radial cracks: the onset of damage corresponds with changes in moisture content, starting from the surface region. Afterwards,

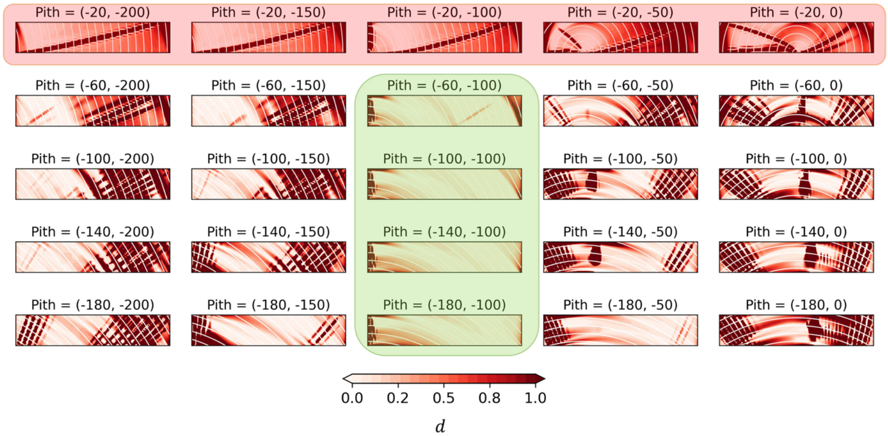

Fig. 18 Damage parameter d for tangential direction (see Eq. 7) of boards with different pith coordinate (y, z)

due to the damage, the affected areas can withstand less stress, leading to stress redistribution inside the entire board. Given the low tensile strength in the tangential direction, significant tangential damage is then formed and evolves in the radial direction.

The damage pattern in different boards varies significantly due to the location of the pith. As shown in the green box in Fig. 18, for boards where the z-coordinate of the pith is near the surface region (i.e., pith = (y, z), with $y \leq -60$ mm, $z \approx -100$ mm), the damage remains localized at the surface, since the penetration direction is almost vertical. Conversely, as highlighted in the red box, for boards where the y-coordinate is within the thickness of the board (i.e., pith = (y, z), $-20 \leq y \leq 0$ mm), the damage progresses almost horizontally, penetrating the entire width of the board. In such cases, serious concerns can be raised about the stability of the entire glulam structure.

Conclusion

This study employed Monte Carlo simulations to analyze moisture-induced stress in glulam, where the pith locations of different layers are taken as the input random variables. Three key observations can be concluded from the Monte Carlo results:

1. The moisture-induced stress varies significantly among boards with different pith locations, highlighting the importance of considering the growth-ring effect.
2. The influence of neighboring board types on shrinkage stress is minimal, suggesting that focusing on features of the analyzed layer itself rather than neighboring layers is sufficient in many cases.

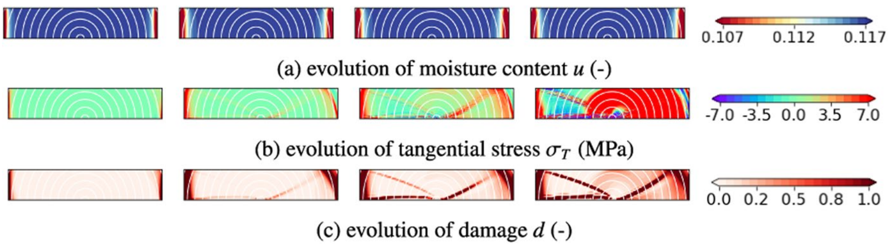

Fig. 19 Damage evolution of board with pith of (− 20 mm, 0 mm) after 36, 100, 104, 106 h

3. A strong non-linear correlation exists between the moisture-induced stress and the material rotational angle in the surface region.

To address the need for reducing computational costs and understanding of how material parameters influence moisture-induced stress, two levels of simplification methods are proposed based on the observations. These methods yield the following insights:

1. The nonlinear relationship between moisture-induced stress and material parameters can be approximated by mathematical equations;
2. The common assumption - a board with pith at the middle of its bottom surface represents the most critical case - holds true if $\frac{E_T\alpha_T}{f_T} > \frac{E_R\alpha_R}{f_R}$;
3. Spruce and larch are more sensitive to moisture fluctuations compared to beech and pine, according to the material parameters provided in literature;
4. In the analyzed example of beech, moisture-induced damage primarily advances in the radial direction.
5. Although damage is initiated by the moisture-induced stress that is localized at the surface region, the advancement of damage can penetrate the entire width of the board, for boards where the height of pith is within the board's thickness.

Author Contributions Taoyi Yu: Conceptualization, Methodology, Software, Writing—original draft, Writing—review & editing. Franziska Seeber: Methodology, Software, Writing—review & editing. Ani Khaloian: Conceptualization, Methodology, Writing—review & editing, Supervision, Project administration, Funding acquisition. Jan-Willem van de Kuilen: Conceptualization, Writing—review & editing, Supervision, Project administration, Funding acquisition.

Funding Open Access funding enabled and organized by Projekt DEAL.

Data Availability No datasets were generated or analysed during the current study.

Declarations

Conflict of interest The authors declare no Conflict of interest.

Open Access This article is licensed under a Creative Commons Attribution 4.0 International License, which permits use, sharing, adaptation, distribution and reproduction in any medium or format, as long as you give appropriate credit to the original author(s) and the source, provide a link to the Creative Commons licence, and indicate if changes were made. The images or other third party material in this article are included in the article's Creative Commons licence, unless indicated otherwise in a credit line to the material. If material is not included in the article's Creative Commons licence and your intended use is not permitted by statutory regulation or exceeds the permitted use, you will need to obtain permission directly from the copyright holder. To view a copy of this licence, visit http://creativecommons.org/licenses/by/4.0/.

References

Aicher S, Dill-Langer G (2005) Effect of lamination anisotropy and lay-up in glued-laminated timbers. J Struct Eng 131(7):1095–1103

Autengruber M, Lukacevic M, Gröstlinger C, Füssl J (2021) Finite-element-based prediction of moisture-induced crack patterns for cross sections of solid wood and glued laminated timber exposed to a realistic climate condition. Constr Build Mater 271:121775

Avramidis S (1989) Evaluation of three-variable models for the prediction of equilibrium moisture content in wood. Wood Sci Technol 23(3):251–257

Brandstätter F, Autengruber M, Lukacevic M, Füssl J (2023) Prediction of moisture-induced cracks in wooden cross sections using finite element simulations. Wood Sci Technol 57(3):671–701

Bucur V (2011) Delamination in wood. Wood products and wood-based composites. Springer, Netherlands

Dietsch P, Gamper A, Merk M, Winter S (2015) Monitoring building climate and timber moisture gradient in large-span timber structures. J Civ Struct Heal Monit 5(2):153–165

Florisson S, Gamstedt EK (2023) An overview of lab-based micro computed tomography aided finite element modelling of wood and its current bottlenecks. Holzforschung 77(11–12):793–815

Florisson S, Ormarsson S, Vessby J (2019) A numerical study of the effect of green-state moisture content on stress development in timber boards during drying. Wood Fiber Sci 51(1):41–57

Fortino S, Hradil P, Genoese A, Genoese A, Pousette A (2019) Numerical hygro-thermal analysis of coated wooden bridge members exposed to northern European climates. Constr Build Mater 208:492–505

Fortino S, Mirianon F, Toratti T (2009) A 3d moisture-stress fem analysis for time dependent problems in timber structures. Mech Time Depend Mater 13(4):333–356

Franke B, Franke S, Müller A, Schiere M (2016) Long-term behaviour of moisture content in timber constructions-relation to service classes. Int Netw Timber Eng Res Meet 49(5):19–23

Franke S, Franke B, Harte AM (2015) Failure modes and reinforcement techniques for timber beams—state of the art. Constr Build Mater 97:2–13

Hassani MM (2015) Adhesive bonding of structural hardwood elements. Doctoral dissertation, ETH Zurich

Hassani MM, Wittel FK, Hering S, Herrmann HJ (2015) Rheological model for wood. Comput Methods Appl Mech Eng 283:1032–1060

Huber J, Ekevad M, Broman O (2021) Using computed tomography data for finite element models of wood boards. In: 14th WCCM-ECCOMAS congress. CIMNE

Jönsson J, Thelandersson S (2003) The effect of moisture gradients on tensile strength perpendicular to grain in glulam. Holz als Roh- und Werkstoff 61(5):342–348

Lee SS, Pan SJ, Jeong GY (2019) Effects of size, species and adjacent lamina on moisture related strain in glulam. Wood Fiber Sci 51(2):101–118

Lukacevic M, Kandler G, Hu M, Olsson A, Füssl J (2019) A 3d model for knots and related fiber deviations in sawn timber for prediction of mechanical properties of boards. Mater Des 166:107617

Lukacevic M, Lederer W, Füssl J (2017) A microstructure-based multisurface failure criterion for the description of brittle and ductile failure mechanisms of clear-wood. Eng Fract Mech 176:83–99

Ormarsson S, Dahlblom O, Petersson H (1998) A numerical study of the shape stability of sawn timber subjected to moisture variation part 1: theory. Wood Sci Technol 32(5):325–334

Ormarsson S, Gíslason ÓV (2016) Moisture-induced stresses in glulam frames. Eur J Wood Wood Prod 74(3):307–318

Pěnčík J (2015) Tests of wooden specimens from scots pine (*Pinus sylvestris*) with the help of anisotropic plasticity material model. Drvna industrija 66(1):27–33

Qiu L (2015) Performance of curved glulam beams under load and moisture variations: Doctoral dissertation. Harbin, China

Seeber F, Khaloian-Sarnaghi A, Rais A, van de Kuilen J-W (2023) A numerical strength prediction approach for wood using element-wise local fiber directions from laser scanning. Mater Des 226:111578

Seeber F, Khaloian-Sarnaghi A, Yu T, Duddeck F, van de Kuilen J-W (2024) Development and validation of an orthotropic 3d elasto-plastic damage model for wood, considering fiber deviations. Eng Struct 308:117928

van der Velden A, Kuipers J (1976) Directives for the fabrication of load-bearing structures of glued timber. In CIB-W18 meeting

Yu T, Khaloian A, van de Kuilen J-W (2022) An improved model for the time-dependent material response of wood under mechanical loading and varying humidity conditions. Eng Struct 259:114116

Yu T, Khaloian-Sarnaghi A, Seeber F, van de Kuilen J-W (2023) Stochastic FE analysis of stress concentrations in curved glulam beams due to the uncertainty of material direction. Constr Build Mater 393:131537

Zhou H, Zhu E, Fortino S, Toratti T (2010) Modelling the hygrothermal stress in curved glulam beams. J Strain Anal Eng Des 45(2):129–140

Publisher's Note Springer Nature remains neutral with regard to jurisdictional claims in published maps and institutional affiliations.